

Radiative Acceleration and X-ray Spectrum of Outflowing Pure Electron-Positron Pair Fireball in Magnetar Bursts

TOMOKI WADA ¹ AND KATSUAKI ASANO¹

¹*Institute for Cosmic Ray Research, The University of Tokyo, Kashiwa, Chiba, Japan*

ABSTRACT

One X-ray short burst accompanied by a Galactic fast radio burst has been detected so far, and its X-ray cut-off energy was significantly higher than that of other X-ray short bursts. Such X-ray bursts are thought to be emitted from a fireball in the magnetosphere of magnetars. If a fireball is formed around a magnetic pole, it expands and is accelerated under its radiation pressure, later producing photon emission and plasma outflow, which can be responsible for radio bursts. We numerically study the radiative acceleration of this outflowing fireball, which consists of electron-positron pairs and radiation, and obtain the spectrum of the escaped X-ray photons. We consistently take into account cyclotron resonant scattering, which enhances the scattering cross section resulting in a strong radiative force and high optical depth. Our results show that similar spectra to the observed X-ray spectrum in the Galactic fast radio burst are realized in outflowing fireballs and that the plasma outflow is simultaneously accelerated to a high Lorentz factor owing to cyclotron resonant scattering.

1. INTRODUCTION

Magnetars are neutron stars with photospheric luminosities higher than their spin-down luminosities (e.g., Harding & Lai 2006; Kaspi & Beloborodov 2017; Enoto et al. 2019, for reviews). Their spin-down luminosities indicate that the magnetars have strong magnetic field of $\sim 10^{14}$ – 10^{15} G, which are considered to be the energy source of the high photospheric luminosities (Duncan & Thompson 1992). Magnetars frequently exhibit bursting activities, short bursts, outbursts, and flares. The duration of short bursts and flares is roughly about 1 s, and they are categorized by the total luminosity ($\lesssim 10^{44}$ erg s⁻¹ for the short bursts, and $\gtrsim 10^{44}$ erg s⁻¹ for the flares; Kaspi & Beloborodov 2017). The short bursts and the flares are considered to be triggered by a sudden release of their magnetic energy (Thompson & Duncan 1995, 1996). The released energy is soon thermalized; an electron-positron pair plasma tightly coupled with photons, so-called a fireball, is formed. X-ray photons of short bursts and flares are emitted from this fireball.

The fireball dynamics and X-ray spectrum depend on the shape of the magnetic field at the largest scale and on the ratio of the thermal energy density to the magnetic energy density. (1) Trapped fireball: If the fireball is formed far from the magnetic pole and the thermal energy density is much lower than the magnetic energy density, the fireball would be trapped in a closed magnetic flux tube. The photon energy escaping from the

trapped fireball is typically ~ 10 keV (see Thompson & Duncan 1995 for details). The X-ray spectrum of the emission from the trapped fireball has been studied, and some observed X-ray spectra of short bursts are reproduced (Lyubarskii 1986; Lyubarsky 2002; Yamasaki et al. 2020). The polarization of the X-ray emission is also studied in Yang & Zhang (2015). (2) Expanding fireball: If the thermal energy density is much higher than the magnetic energy density, the fireball would not be confined in the magnetic flux tube and would expand unaffected by the magnetic field. This type of fireball may be realized in the initial spike of the magnetar flares (Thompson & Duncan 1995, 2001). In this case, the X-ray spectrum is almost blackbody, which agrees with the observed magnetar flare properties (Hurley et al. 1999, 2005; Boggs et al. 2007). (3) Outflowing fireball: Even if the released energy is much lower than the magnetic energy, an energy release near the magnetic pole may form an outflowing fireball. The fireball confined in the open magnetic flux tube would expand along the flux tube (Thompson & Duncan 2001). For this case, the X-ray spectrum and polarization are numerically studied in van Putten et al. (2016) under a given non-relativistic fluid profile.

The expanding/outflowing fireball in magnetar short bursts may be the source of fast radio bursts (FRBs). FRBs are bright radio bursts with a duration of a few milliseconds (Lorimer et al. 2007; Thornton et al. 2013). The number of detected FRBs so far is more than 800,

but their source and the emission mechanism of coherent radio waves are unknown (Katz 2018; Cordes & Chatterjee 2019; Platts et al. 2019; Petroff et al. 2019; Zhang 2020a,b; Lyutikov 2021; Platts et al. 2021; Petroff et al. 2021, for reviews). The origin of almost all FRBs is extragalactic, but there is one exception, FRB 20200428A (Bochenek et al. 2020; CHIME/FRB Collaboration et al. 2020). FRB 20200428A came from a Galactic magnetar, SGR1935+2154, and was associated with hard X-ray short bursts (Mereghetti et al. 2020; Li et al. 2021; Ridnaia et al. 2021; Tavani et al. 2021; Li et al. 2022). This event implies that at least a fraction of FRBs accompany X-ray short bursts, but the physical connection between FRBs and X-ray bursts, even the energy budget, is still under debate (e.g., Lu et al. 2020; Katz 2020; Ioka 2020; Yang & Zhang 2021; Yamasaki et al. 2022).

FRBs may be emitted from a relativistically outflowing plasma driven by expanding/outflowing fireballs (Yang & Zhang 2021; Wada & Ioka 2023). In an optically thick region, the relativistic outflow is accelerated by an isotropic radiation pressure. This acceleration mechanism has been studied in the fireball model of gamma-ray bursts (Goodman 1986; Paczynski 1986; Shemi & Piran 1990, and Piran 1999; Zhang 2018 for reviews). Even in an optically thin region, if the radiation luminosity is much higher than the kinetic luminosity of the plasma, the plasma outflow is further accelerated by radiative force (Grimsrud & Wasserman 1998; Meszaros et al. 1993; Nakar et al. 2005; Chhotray & Lazzati 2018). In addition to the fireball model of the gamma-ray bursts, this acceleration mechanism has been discussed in the context of the relativistic outflow from active galactic nuclei as well (Iwamoto & Takahara 2004; Asano & Takahara 2007, 2009). X-ray photons, responsible for the radiative acceleration in magnetar bursts, can be resonantly scattered at the radius where the typical photon energy equals the cyclotron energy determined by the magnetic field. Thus, this resonant scattering effect should be taken into account to evaluate the dynamics of the relativistic plasma outflow (Wada & Ioka 2023).

In this paper, we numerically demonstrate that plasma outflows are accelerated up to an ultra-relativistic speed (the Lorentz factor is $\mathcal{O}(10^2)$) by the radiative force via cyclotron resonant scattering, and obtain photon spectra similar to the observed X-ray spectrum of the short burst associated with the FRB 20200428A. We solve the radiation hydrodynamic equations numerically under the assumption that the fireball is composed of an electron-positron pair plasma and the flow is spherically symmetric and steady. Wada & Ioka (2023) shows that the kinetic energy of the outflow

driven by a “pure” electron-positron pair fireball is not sufficient for the energy budget for the observed FRB. However, it is suggested that the relativistic outflow in a baryon-loading fireball can energize FRBs. The Lorentz factor of the baryon-loading fireball is lower than the pair fireball due to the higher mass density, but only by a factor of ~ 2 . Wada & Ioka (2023) also derive analytical expressions for the terminal Lorentz factor of the outflows. In this paper, we verify their analytical solutions with numerical simulations. We solve both the radiation and plasma outflows and provide steady solutions for them.

This paper is organized as follows. In Section 2, we describe the method and the boundary condition for the numerical simulations. In Section 3, we present results of the numerical simulations. In Section 3.1, we show that the observed X-ray spectrum is reproduced under a certain boundary condition, and a relativistic plasma outflow is also created by the resonant scattering in the magnetized pair plasma. In Section 3.2, we show the parameter dependence of the radiative acceleration and the photon spectrum. Section 4 is devoted to the conclusions and discussion. We use $Q_x = Q/10^x$ in cgs units unless otherwise noted.

2. METHOD

2.1. Physical Setup

An outflowing fireball along an open flux tube is created in a magnetar short burst if significant energy is injected at the bottom of the open magnetic field lines. The energy injection may be from a trapped fireball, which is trapped in the closed magnetic field lines and does not expand (Thompson & Duncan 2001; Ioka 2020; Yang & Zhang 2021; Demidov & Lyubarsky 2023). As the fireball expands along the flux tube, it is adiabatically cooled, the number density of the plasma decreases, and finally the fireball becomes optically thin to the Thomson scattering. Photons are initially escaped around this photospheric radius, r_{ph} , where the optical depth for the Thomson scattering equals unity (see Figure 1). Note that r_{ph} is defined for the usual Thomson cross section in this paper. The escaped photons will be observed as X-ray short bursts.

Even above this photospheric radius, the outflow can be accelerated by the radiative force. The force is proportional to the product of the photon flux and the cross section (e.g., Sec 6.4 of Mihalas & Mihalas 1984). If the luminosity of photons is higher than the kinetic luminosity of the plasma, the number of photons is much larger than that of the plasma. Most photons are not scattered by the plasma, but plasma particles are continuously scattered by photons. As a result, the plasma

is subjected to the radiative force and is accelerated (Meszaros et al. 1993; Grimsrud & Wasserman 1998; Li & Sari 2008; Asano & Takahara 2009).

In a magnetic field, photons can be resonantly scattered with a larger cross section than the Thomson cross section. This cyclotron resonant scattering occurs at the radius where $\omega = \omega_B$ is satisfied. Here, ω is the angular frequency of a photon, $\omega_B = \hbar e B / mc$ is the cyclotron frequency, \hbar is the reduced Planck constant, e is the elementary charge, B is the magnetic field, m is the electron mass, and c is the speed of light. Because of the large cross section, the radiative force via the resonant scattering is stronger than the radiative force via the usual Thomson scattering. Thus, the plasma outflow is accelerated up to a higher Lorentz factor by the resonant scattering. Additionally, the photon spectrum can be modified by the resonant scattering above r_{ph} (e.g., Yamasaki et al. 2020).

We study both the radiative acceleration above the photospheric radius and the Comptonized photon spectrum consistently assuming a spherically symmetric steady flow. Below the photospheric radius, photons and electron-positron pairs are strongly coupled and follow the hydrodynamic equations with an adiabatic index of $4/3$. Around the photospheric radius, the pair annihilation freezes out, and the numbers of photons and electron-positron pairs will not change above this radius (e.g. Asano & Takahara 2009). Above the photospheric radius, photons follow the radiative transfer equation and the electron-positron pairs follow the hydrodynamic equations. We solve the radiative transfer equation in the magnetized plasma and the equation of motion of the plasma iteratively and obtain steady-state solutions.

In this paper, we consider fireballs composed of electron-positron pairs, and baryons are not included for simplicity. If baryons are loaded on the fireball, there would be two main differences as follows. First, the terminal velocity of the outflow would be lower than the result of this paper. Second, the eigenmodes of electromagnetic waves in the plasma with baryons are circularly polarized, while the eigenmodes in the pair plasma are linearly polarized. The scattering cross sections for these modes are also different, and so the difference due to these eigenmodes may alter the propagation of photons. The baryon-loaded fireball will be studied in our future papers.

Photons follow the radiation transfer equation with the scatterings in a magnetized electron-positron pair plasma. In general the radiation transfer equation is (e.g., Lindquist 1966; Mihalas & Mihalas 1984, and

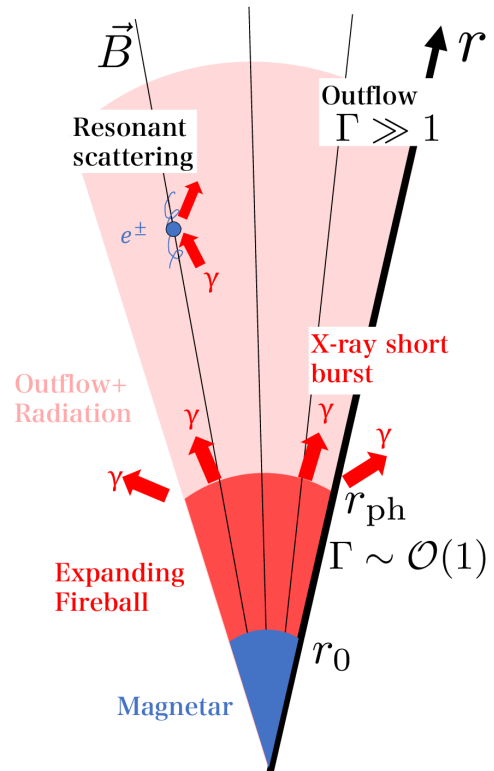


Figure 1. Schematic picture of the outflowing pair fireball. From the magnetar surface at $r = r_0$, an optically thick fireball expands to the photospheric radius, $r = r_{\text{ph}}$. The pair creation and annihilation are almost negligible above the photospheric radius, and almost all photons are not scattered via the Thomson scattering above this radius. We conduct the numerical simulation from this radius. As photons propagate, the magnetic field decreases, and the photons undergo the resonant scattering where its frequency equals the cyclotron frequency. Photons are Comptonized by the resonant scattering. As the backreaction of this scattering, the outflow is accelerated.

(Sasaki 1958, 1962 for mathematical formulation)

$$p^\mu \left(\frac{\partial}{\partial x^\mu} - \Gamma_{\mu\nu}^\rho p^\nu \frac{\partial}{\partial p^\rho} \right) F_\gamma(x^\mu, \mathbf{p}) = \left(\frac{dF_\gamma}{d\lambda} \right)_{\text{coll}}, \quad (1)$$

where \mathbf{p} is the spacial component of the four-momentum of photons p^μ , x^μ is the space coordinates, $\Gamma_{\mu\nu}^\rho$ is the Christoffel symbol, $F_\gamma(x^\mu, \mathbf{p})$ is the distribution function of photons, $\left(\frac{dF_\gamma}{d\lambda} \right)_{\text{coll}}$ is the collision term, and λ is the affine parameter. We solve Equation (1) by Monte-Carlo scheme in the plasma flow obtained by the fluid simulation.

As the strong synchrotron cooling would force electrons and positrons in the ground state of the Landau level, the equation of motions for a relativistic pair outflow should take into account anisotropic pressure. The

energy-momentum conservation is

$$\nabla_\mu T^{\mu\nu} = -\nabla_\mu R^{\mu\nu}, \quad (2)$$

where ∇_μ is covariant derivative with respect to x^μ , $T^{\mu\nu}$ is the energy-momentum tensor of the anisotropic fluid, and $R^{\mu\nu}$ is that of the radiation. The radiative force, $-\nabla_\mu R^{\mu\nu}$, is evaluated using the solution of the radiation transfer equation (Equation (1)). Neglecting electron-positron pair annihilation/creation, the mass flux conservation is written as

$$\nabla_\mu(\rho u^\mu) = 0, \quad (3)$$

where ρ is the comoving rest-mass energy density of the plasma, and u^μ is the four-velocity of it (see Section 2.2 for details). We solve Equations (2) and (3) under the radiative force obtained by the radiation simulation.

For simplicity, we assume a spherically symmetric steady flow and neglect the gravity of the magnetar. The direction of the magnetic field is also assumed to be radial. We also assume that photons are not absorbed nor produced above the photospheric radius, and that the fireball below the photospheric radius is a thermalized electron-positron pair plasma and photons (see Section 2.4).

2.2. Hydrodynamics of Anisotropic Plasma

The energy-momentum tensor of the anisotropic plasma is given as follows (Chew et al. 1956; Gedalin 1991; Gedalin & Oiberman 1995),

$$T^{\mu\nu} = (\rho h + P_\perp)u^\mu u^\nu + P_\perp g^{\mu\nu} + (P_\parallel - P_\perp)\hat{b}^\mu \hat{b}^\nu, \quad (4)$$

where h is the specific enthalpy of the fluid, P_\perp is the pressure perpendicular to the magnetic field, P_\parallel is the pressure parallel to the magnetic field, $g^{\mu\nu}$ is the metric of the spacetime, and \hat{b}^μ is a tetrad whose spatial direction is parallel to the magnetic field in the comoving frame of the fluid. The fluid flows along the radial flux tube, and the magnetic pressure does not exert any force on the fluid. The specific enthalpy is expressed as

$$h = 1 + \frac{e_{\text{th}}}{\rho} + \frac{P_\perp}{\rho}, \quad (5)$$

where e_{th} is the thermal energy of the fluid. In the case that the synchrotron cooling timescale is much shorter than the timescale for the isotropization of the plasma, particles are at the ground state of the Landau level, and thus,

$$P_\perp = 0. \quad (6)$$

Therefore, the energy-momentum tensor of the anisotropic plasma in this case is

$$T^{\mu\nu} = \rho h u^\mu u^\nu + P_\parallel \hat{b}^\mu \hat{b}^\nu. \quad (7)$$

We solve Equation (2) with this energy-momentum tensor.

For the spherically symmetric flow, we use the polar coordinates (t, r, θ, ϕ) , where the components of the metric is

$$g_{\mu\nu} = \text{diag}(-c^2, 1, r^2, r^2 \sin^2 \theta), \quad (8)$$

and then, the components of u^μ and \hat{b}^μ are

$$u^\mu = (\Gamma, \Gamma\beta, 0, 0), \quad (9)$$

$$\hat{b}^\mu = (\Gamma\beta, \Gamma, 0, 0), \quad (10)$$

where β is the radial velocity of the fluid normalized by the speed of the light, and $\Gamma = (1 - \beta^2)^{-1/2}$. Substituting Equations (9) and (10) into Equation (7), the components of the energy-momentum tensor of the plasma are

$$T^{tt} = \rho h_\parallel \Gamma^2 - P_\parallel, \quad (11)$$

$$T^{tr} = \rho h_\parallel \Gamma^2 \beta, \quad (12)$$

$$T^{rr} = \rho h_\parallel \Gamma^2 \beta^2 + P_\parallel, \quad (13)$$

$$T^{ij} = 0 \text{ (others)}, \quad (14)$$

where we define

$$h_\parallel = 1 + \frac{e_{\text{th}}}{\rho} + \frac{P_\parallel}{\rho}, \quad (15)$$

which is the analogy of the specific enthalpy of an isotropic fluid. We employ the Γ -law ideal equation of state,

$$P_\parallel = (\hat{\Gamma} - 1)e_{\text{th}}. \quad (16)$$

For the gas in which the thermal motion of all particles is in one dimension (along the magnetic field line in this case), $\hat{\Gamma}$ equals 3. Using Equations (2), (3), (9), and (11)–(14), the continuity equation and the equation of motions are

$$\partial_t(r^2 \rho \Gamma) + \partial_r(r^2 \rho \Gamma \beta) = 0, \quad (17)$$

$$\partial_t[r^2(\rho h_\parallel \Gamma^2 - P_\parallel)] + \partial_r[r^2 \rho h_\parallel \Gamma^2 \beta] = r^2 G^t, \quad (18)$$

$$\partial_t[r^2 \rho h_\parallel \Gamma^2 \beta] + \partial_r[r^2(\rho h_\parallel \Gamma^2 \beta^2 - P_\parallel)] = r^2 G^r, \quad (19)$$

where ∂_μ denotes the partial differential with respect to x^μ , and $G^\mu = -\nabla_\nu R^{\mu\nu}$ is the radiation four-force density, which is given by the result of the Monte-Carlo calculation (see Section 2.3). Unlike in the case of an isotropic fluid, the pressure does not appear on the right-hand side of Equation (19), because $T^{\theta\theta}$ and $T^{\phi\phi}$ are proportional to P_\perp and $P_\perp = 0$. We solve Equations (17)–(19) numerically.

The numerical method and setup employed in our study are as follows. We adopt the relativistic HLLE

approximate Riemann solver (Einfeldt 1988; Schneider et al. 1993, and Martí & Müller 2003 for a review) and 2nd-order MUSCL reconstruction for the spatial interpolation (van Leer 1979) with the minmod function as a flux limiter (Roe 1986). The time integral is performed with the second-order Runge-Kutta method. Our code successfully passes some shock tube tests in Schneider et al. (1993). We set the CFL number around 10^{-4} – 10^{-3} because the value of the radiative force is larger than that of the energy-momentum flux of the fluid (see Equations (18) and (19)). The radius is divided into about 9000 cells. We check that our simulation result does not change in a higher resolution simulation, in which the cell size is half. To conduct this simulation with a small CFL number, we divide the space into 3–5 parts. From inner parts to outer parts, the calculations are performed until the steady solutions are realized in each part. As we aim to obtain steady solutions, it does not matter if the transient behavior i.e., time-dependence of the solution, is somewhat imprecise.

2.3. Radiation Transfer in a Magnetized Plasma

The scattering effects are included as the collision term in Equation (1). If there is no absorption nor emission process, the collision term is written as (Lindquist 1966)

$$\left(\frac{dF_\gamma}{d\tau}\right)_{\text{coll}} = \frac{\rho(x)}{mc^2} [-\kappa(x, p)F_\gamma(x^\mu, \mathbf{p}) + \int d\Pi' \kappa(x, p') \zeta(x; p' \rightarrow p) F_\gamma(x^\mu, \mathbf{p}')] , \quad (20)$$

where $\rho(x)/mc^2$ is the comoving number density of the plasma, $\kappa(x, p)$ is a invariant scattering opacity, $\zeta(x; p' \rightarrow p)$ is a invariant phase function (e.g., Chandrasekhar 1960), and $d\Pi = p^t dp^t d\Omega$ for photons in a flat spacetime. We denote the solid angle element with $d\Omega$. The first term in the right-hand side of Equation (20) expresses the decrease of the number of photons due to the scattering out of the momentum \mathbf{p} , and the second term expresses the increase due to the scattering from a momentum \mathbf{p}' to the momentum \mathbf{p} . The invariant scattering opacity and the scattering cross section satisfy

$$\kappa(x, p) = p^t \sigma(x, p) , \quad (21)$$

where $\sigma(x, p)$ is the cross section in the frame where p^t is measured. The invariant phase function satisfies

$$\zeta(x; p' \rightarrow p) = \frac{1}{p^t \sigma(x, p')} \frac{d\sigma}{dp^t d\Omega} . \quad (22)$$

The specific expression of the differential cross-section is determined by the plasma physics in the magnetic field.

Electromagnetic waves in an electron-positron pair plasma can be decomposed into two eigenmodes of linearly polarized waves, extraordinary mode (X-mode) and ordinary mode (O-mode) (e.g., Lifshitz & Pitaevskii 1981; Meszaros 1992). The electric field of an O-mode photon is on the plane that contains the wavenumber vector of the photon and the magnetic field. The electric field of an X-mode photon is perpendicular to that plane. The cross sections of X-mode photons and O-mode photons in the frame where the particle motion parallel to the magnetic field equals zero (hereafter denoted as the electron rest frame¹) are written as (e.g., Canuto et al. 1971; Herold 1979; Ventura 1979; Nagel 1981; Meszaros 1992; Yang & Zhang 2015)

$$\frac{d\sigma^{\text{XX}}}{d\Omega} = \frac{3\sigma_{\text{T}}}{32\pi} \left(\frac{1}{(1 + \mathbf{u}^{1/2})^2 + \gamma_e^2} + \frac{1}{(1 - \mathbf{u}^{1/2})^2 + \gamma_e^2} \right) , \quad (23)$$

$$\frac{d\sigma^{\text{XO}}}{d\Omega} = \frac{3\sigma_{\text{T}}}{32\pi} \cos^2 \theta' \left(\frac{1}{(1 + \mathbf{u}^{1/2})^2 + \gamma_e^2} + \frac{1}{(1 - \mathbf{u}^{1/2})^2 + \gamma_e^2} \right) , \quad (24)$$

$$\frac{d\sigma^{\text{OX}}}{d\Omega} = \frac{3\sigma_{\text{T}}}{32\pi} \cos^2 \theta \left(\frac{1}{(1 + \mathbf{u}^{1/2})^2 + \gamma_e^2} + \frac{1}{(1 - \mathbf{u}^2)^{1/2} + \gamma_e^2} \right) , \quad (25)$$

$$\frac{d\sigma^{\text{OO}}}{d\Omega} = \frac{3\sigma_{\text{T}}}{8\pi} \left[\sin^2 \theta \sin^2 \theta' + \frac{\cos^2 \theta \cos^2 \theta'}{4} \times \left(\frac{1}{(1 + \mathbf{u}^{1/2})^2 + \gamma_e^2} + \frac{1}{(1 - \mathbf{u}^{1/2})^2 + \gamma_e^2} \right) \right] , \quad (26)$$

where $d\sigma^{\text{AB}}/d\Omega$ ($A, B = X, O$) is the differential scattering cross section of A-mode photon into B-mode, σ_{T} is the Thomson cross section, θ is the angle between the wavevector of the incident photon and the magnetic field in the electron rest frame, θ' is the angle between the wavevector of the scattered photon and the magnetic field in the electron rest frame, $\mathbf{u} \equiv \omega_B^2/\omega^2$, and $\gamma_e = 2e^2\omega_B/(3mc^3)$ is the radiative damping factor. Here, we neglect the thermal motion of electrons for simplicity (cold approximation), as the temperature of electrons is lower than the rest-mass energy. The cross

¹ Exactly speaking, the electron is not at rest due to the zero-point oscillation at the ground state of the Landau level but we neglect it.

sections of Equations (23)–(26) are used for the collision term of Equation (20).

In the anisotropic plasma we mentioned above, the momentum distribution of electron–positron pairs is one dimensional (Canfield et al. 1987) as

$$f_{\pm,1D}(p_{\parallel}, T_{\parallel}) dp_{\parallel} = \frac{\exp\left(-\frac{\sqrt{m^2c^4 + p_{\parallel}^2c^2}}{T_{\parallel}}\right)}{mcK_1(mc^2/T_{\parallel})} dp_{\parallel}, \quad (27)$$

where p_{\parallel} is the momentum of electrons or positrons parallel to the magnetic field, T_{\parallel} is the kinetic temperature of pairs parallel to the magnetic field, and $K_1(x)$ is the modified Bessel function of the second kind. The parallel temperature T_{\parallel} satisfies (Gedalin 1991),

$$P_{\parallel} = \frac{\rho}{mc^2} T_{\parallel}, \quad (28)$$

where P_{\parallel} and ρ are obtained from the fluid simulation.

In our Monte-Carlo scheme, the radiation field is described by a set of packets (e.g., Pozdnyakov et al. 1983; Dolence et al. 2009; Lazzati 2016; Kawaguchi et al. 2023). Each packet has information on the position (r in one-dimensional simulation), the momentum (p^t, p^r, p^{θ}), and the polarization (X-mode or O-mode). The calculation regime is divided into spherical cells, and the statistical quantities of radiation (the intensity, the radiative force, and so on) are recorded at each cell.

The radiative force G^{ν} is evaluated from the distribution function, $F_{\gamma}(x^{\mu}, \mathbf{p})$ (Lindquist 1966 and see Appendix A) as

$$G^{\nu} = -\frac{\rho(x)}{mc^2} h_{\lambda}^{\nu} \int d\Pi p^{\lambda} \kappa(x, p) F_{\gamma}(x^{\mu}, \mathbf{p}), \quad (29)$$

where $h_{\mu}^{\nu} = \delta_{\mu}^{\nu} + u^{\nu} u_{\mu}$ is the projection tensor onto the 3-space orthogonal to u^{μ} . In this paper, the temperature of the pair plasma is non-relativistic, and we evaluate the collision term in Equation (29) using Equations (23)–(26) without considering the thermal motion of the plasma. In Lindquist (1966), the expression of the radiative force, Equation (29), is derived under the assumption that the scattering is elastic and isotropic. As shown in Appendix A, Equation (29) is valid in the case that the scattering is elastic and the differential scattering cross section is an even function of the direction of the incident and scattered photon. Because Equations (23)–(26) are even functions of $\cos\theta$ and $\cos\theta'$, Equation (29) is applicable. Another method to evaluate the radiative force is to calculate the radiative force with the four-momentum changes in all scattering processes in the Monte-Carlo simulation (e.g., Ryan et al. 2015; Kawaguchi et al. 2023). For steady and

strongly radiation-dominated cases, the expression of Equation (29) would be more useful to reduce Monte-Carlo shot noise. This is because the radiative force in Equation (29) is evaluated using all photon packets and the statistical error is determined by the number of the packets and not by the number of the scattering. Therefore, we adopt Equation (29) as the radiative force.

The scattering process is treated as follows. For a packet in a radial cell, the probability of escaping from the cell is (Abramowicz et al. 1991)

$$\mathcal{P}_{\text{esc}} = 1 - \exp(-\Delta\tau), \quad (30)$$

$$\Delta\tau = \Gamma(1 - \beta \cos\theta_L) \frac{\rho}{mc^2} \sigma^A \Delta l, \quad (31)$$

where $\cos\theta_L$ is the angle between the radial direction and the wavevector of the packet in the lab frame, $\sigma^A = \sum_B \sigma^{AB}$ is the cross section for the packet of A -mode photons and Δl is the distance that the packet must propagate before escaping from the cell in the lab frame. We generate a random variable, ξ , uniformly distributing in $(0, 1]$. If $\xi < \mathcal{P}_{\text{esc}}$, the packet escapes from the current cell. If $\xi > \mathcal{P}_{\text{esc}}$, the packet is scattered in the cell after it propagates

$$\Delta l' = -\frac{\Delta l}{\Delta\tau} \ln[1 - \xi(1 - \exp(-\Delta\tau))], \quad (32)$$

along its trajectory. At the position, we probabilistically choose a pair particle from the one-dimensional distribution function (see Equations (27) where T_{\parallel} is given by the fluid calculation). Next, in the rest frame of that particle, we probabilistically determine both the direction and the mode of the scattered packet using Equations (23)–(26). Finally, we translate the angle and the four-momentum of that scattered packet to those in the lab frame, and again calculate the probability of escaping from the cell with a newly generated random variable ξ' . We continue these processes until the photon escapes from the computational domain.

The adopted parameters and numerical scheme are summarized as follows. Equation (1) with the scattering term, Equations (20) and (23)–(26), are solved numerically by the Monte-Carlo scheme. In the numerical calculation, the packet propagation is calculated geometrically, not by solving geodesic equations. We set the number of packets to be 10^6 in the following simulations. We have checked some of our results with higher packet number simulations with 10^7 . We also checked that our code reproduces the inverse-Comptonized spectrum (without fluid motion and with 3D particle distribution) in Pozdnyakov et al. (1983), and reproduces the beaming factor in a relativistic outflow (with isotropic scattering and 3D particle distribution) studied in Beloborodov (2011). We also checked that the ratio of the

energy-momentum tensor (with isotropic scattering and 3D particle distribution) in optically thick limit equals that of the Eddington approximation. In the numerical simulation, we artificially increase γ_e by 300 keeping the total cross section constant, i.e., widening the Lorentzian function in order to reduce the Monte-Carlo shot noise in the radiative force. We found that results do not change without the widening and with more number of packets 10^8 in some of our simulations.

2.4. Boundary Condition

The boundary condition to solve the fluid and radiation is given as follows (see Figure 1). At the magnetar surface, $r = r_0$, we set photon luminosity L_γ , initial fireball size $r_0\theta_0$, and the magnetic field at the surface B_0 . We set r_0 as 10^6 cm. The initial temperature of the fireball, T_0 is determined by

$$L_\gamma = \pi(r_0\theta_0)^2 a_{\text{rad}} T_0^4 c \Gamma_0^2, \quad (33)$$

where a_{rad} is the radiation constant, and Γ_0 is the initial Lorentz factor. Assuming that the sonic point is near the surface, the initial velocity of the fireball at the magnetar surface is set to the sound velocity of the radiation-dominated fluid, $\beta_0 = 1/\sqrt{3}$.

Initially, the fireball is optically thick and treated as a radiation-dominated one-component fluid. For a given boundary condition, we solve the steady flow of the radiation-dominated fluid from $r = r_0$ to the photospheric radius, r_{ph} , at which

$$\tau = \sigma T n_\pm(r_{\text{ph}}, B(r_{\text{ph}})) \frac{r_{\text{ph}}}{\Gamma(r_{\text{ph}})} = 1, \quad (34)$$

where $n_\pm(r, B)$ is the electron-positron pair number density in thermodynamic equilibrium (e.g., [Thompson & Duncan 1995](#)). In calculating this optically thick regime, we neglect the contribution of the rest mass density of the plasma to the specific enthalpy. Using the temperature at the photospheric radius, T_{ph} , and the velocity at the photospheric radius, β_{ph} , the boundary condition of the anisotropic fluid is evaluated. The initial density of the plasma is given by solving Equation (34) with $n_\pm = \rho(r_{\text{ph}})/(mc^2)$. The initial velocity of the plasma, $\beta(r_{\text{ph}})$, is β_{ph} . The kinetic temperature of the fluid, T_{\parallel} , is set to the temperature of the radiation-dominated fluid, i.e., $T_{\parallel}(r_{\text{ph}}) = T_{\text{ph}}$. Other boundary conditions are given by using Equations (15), (16), and (28).

The boundary condition for the photon field is also given at r_{ph} . The photon number flux at r_{ph} is

$$\dot{N}_\gamma = 4\pi f_b r_{\text{ph}}^2 \frac{2\bar{\zeta}(3)}{\pi^2} \left(\frac{T_{\text{ph}}}{\hbar c}\right)^3 c \Gamma(r_{\text{ph}})^2, \quad (35)$$

where N_γ is the total number of photons, $\bar{\zeta}(z)$ is the zeta function, and f_b is the beaming factor for photons

denoted as the ratio of the solid angle with the polar angle θ_0 to the one with the polar angle $\theta_0 + \Gamma(r_{\text{ph}})^{-1}$,

$$f_b = \frac{\sin^2(\theta_0/2)}{\sin^2[(\theta_0 + \Gamma(r_{\text{ph}})^{-1})/2]}. \quad (36)$$

The beaming factor is introduced because some photons escape from the conical region in the simulation due to the weak beaming ($\Gamma(r_{\text{ph}}) = \mathcal{O}(1)$) at $r = r_{\text{ph}}$. For the initial photon spectrum, we consider two cases. The first one is the blackbody spectrum with temperature equals T_{ph} ,

$$\frac{dn_\gamma}{d\omega} \propto \frac{\omega^2}{\exp(\omega/T_{\text{ph}}) - 1}, \quad (37)$$

where n_γ is the number density of photons. The second one is the modified blackbody spectrum ([Lyubarsky 2002](#)),

$$\frac{dn_\gamma}{d\omega} \propto \omega^2 \left[\exp\left(\frac{\omega^2}{T_{\text{ph}} \sqrt{\omega^2 + (3\pi^2/5)T_{\text{ph}}^2}}\right) - 1 \right]^{-1} \quad (38)$$

The modified blackbody spectrum is realized if the cyclotron energy at r_{ph} is much higher than the temperature. In the case of $\omega \ll \omega_B$, the cross section of the X-mode photons is proportional to $(\omega/\omega_B)^2$. Thus, photons with lower energy are less frequently scattered, and escape from the inner region of the fireball with a higher intensity. As a result, the emergent photon spectrum is softer than the blackbody spectrum.

In both the two spectra, the initial numbers of photons in X- and O-mode are set equal in our simulations. The initial direction of photons is randomly determined from a uniform distribution of a solid angle in the comoving frame of the plasma. The initial energy of photons is uniformly sampled in logarithmic bins ranging from $10^{-15}T_{\text{ph}}$ to 10^2T_{ph} .

The radial dependence of the magnetic field is set as follows. We assume that the magnetic field is proportional to r^{n_B} as

$$B(r) \propto B_0 \left(\frac{r}{r_0}\right)^{n_B}, \quad (39)$$

where $n_B = -2$ for a split monopole field and $n_B = -3$ for a dipolar field. We perform the numerical simulation up to $r = 1000r_0$, which would be inside the light cylinder of the magnetar. The models with $n_B = -3$ are not consistent with the assumption of the spherically symmetric outflow. However, near the magnetic pole, as long as the angle from the pole is much smaller than 1 rad, the θ -component of the dipole magnetic field is much smaller than the radial component and the outflow flows almost radially. This may justify our calculation for the case of $n_B = -3$.

3. RESULTS

We simulate 5 models as shown in Table 1. In the model **fiducial**, the parameters are chosen to reproduce the observed X-ray spectrum, and the initial spectrum is the modified blackbody spectrum (see Equation (38)). From the model **fiducial**, we change the setup of the simulations as follows. In the model **iso_BB**, we change the initial spectrum into the usual blackbody spectrum (see Equation (37)), and artificially set the scattering to be an isotropic scattering with the Thomson cross section neglecting the effect of the magnetic field. In the model **BB**, we change only the initial spectrum into the blackbody. In the model **B_1e16**, we increase the magnetic field at the surface as 1×10^{16} G. In the model **n_-2**, we change the configuration of the magnetic field from $\propto r^{-3}$ to r^{-2} (see Equation (39)).

3.1. Radiative Acceleration and X-ray Spectrum

Figure 2 shows the four-velocity for the models **fiducial** and **iso_BB**. The outflow is accelerated by the radiative force even in the optically thin region following $\Gamma\beta \propto r$ (Meszaros et al. 1993; Grimsrud & Wasserman 1998; Li & Sari 2008). In both the two models, the terminal four-velocity is much higher than the velocity at the photospheric radius, $\Gamma\beta \sim 1$. The acceleration ends at the radius where the work done by the radiative force during the dynamical timescale gets lower than the rest mass energy of the outflow (see Section 3.3 for details). This condition is satisfied around $r/r_0 \sim 90$ ($\Gamma\beta \sim 100$) in the model **fiducial** (see Equation (48)), and around $r/r_0 \sim 10$ ($\Gamma\beta \sim 10$) in the model **iso_BB** (see Equation (43)). This difference is due to neglecting the resonant scattering in the model **iso_BB**. The resonant scattering is crucial for the creation of the ultra-relativistic outflows with $\Gamma \sim 100$ from magnetars.

The outflow at different radii is accelerated by photons with different energies, $\hbar\omega_o$. Because the magnetic field is proportional to r^{n_B} (see Equation (39)), the cyclotron energy is also proportional to r^{n_B} . On the other hand, the photon energy in the comoving frame of the plasma is $\hbar\omega \sim \hbar\omega_o/\Gamma$, where Γ is proportional to r in the accelerated region and constant in the coasting phase. Photons are resonantly scattered at the radius where $\hbar eB_0(r/r_0)^{n_B}/(mc) \sim \hbar\omega_o/\Gamma$ is satisfied. During the acceleration, the resonant radius is

$$\frac{r_{\text{res}}}{r_0} \sim \left[\frac{eB_0 r_0 \Gamma_{\text{ph}}}{mc\omega_o r_{\text{ph}}} \right]^{1/(-n_B-1)} \sim 5 B_{0,14.3}^{1/2} (\hbar\omega_o)_{100 \text{ keV}}^{-1/2}, \quad (40)$$

where $(\hbar\omega_o)_{100 \text{ keV}} = \hbar\omega_o/100 \text{ keV}$. We have set $\Gamma_{\text{ph}} r_0/r_{\text{ph}} \sim 1$ for simplicity, and set $n_B = -3$ at the

last expression. In the model **fiducial**, the outflow is accelerated by the radiative force via the resonant scattering in $5 \lesssim r/r_0 \lesssim 50$ (see the difference between the red line and the black line in Figure 2), and photons of $100 \text{ keV} \gtrsim \hbar\omega_o \gtrsim 6 \text{ keV}$ sequentially contribute to this acceleration. This radial dependence of the cross section suggests that the terminal velocity also depends on the photon spectrum (see Section 3.2).

Figure 3 shows the X-ray spectrum in the model **fiducial**, which is in agreement with the observation. The X-ray spectrum is calculated under the assumption that photons come from a spherically symmetric shell, on which the intensity and the Lorentz factor are evaluated from the numerical simulation. Above the photospheric radius of the Thomson scattering, the photons are up-scattered in the relativistic outflow, resulting in the observed X-ray spectrum. The pure modified blackbody spectrum is inconsistent with the observation.

The spectrum may be further broadened by considering the structure of the fireball (Lundman et al. 2013; Ito et al. 2013) or the baryons loading (Ryde et al. 2017), both of which are not taken into account in this paper. If these effects are taken into account, the X-ray spectrum may be in even better agreement with the observation.

3.2. Parameter Dependences of the Radiative Acceleration

Figure 4 shows the velocity of the outflow for all the models (see Table 1). The diverse radial dependence of the velocity is created by the resonant scattering and the different photon spectra. The terminal velocity of the model **BB** is a bit lower than that of the model **fiducial**. The cyclotron frequency decreases as $\omega_B \propto B \propto r^{-3}$ with increasing radius. So, at a larger radius, lower energy photons are resonantly scattered and contribute to the radiative force. The photon number density in the low energy region ($\omega \ll T_{\text{ph}}$) is lower in the blackbody spectrum ($dn_\gamma/d\omega \propto \omega$; see Equation (37)) than in the modified blackbody spectrum ($dn_\gamma/d\omega \propto \omega^0$; see Equation (38)). Therefore, at large radii, the radiative force via resonant scattering is weaker in the usual blackbody spectrum than in the modified blackbody spectrum resulting in the lower velocity in the model **BB** than in the model **fiducial**. However, the photon index difference of 1 does not make a significant difference to the terminal velocity in these models.

The terminal velocity of the model **B_1e16** is higher than that of the model **fiducial**. In the model **B_1e16**, the cyclotron energy is higher at a given radius. Photons with higher energies are resonantly scattered, and the higher specific luminosity contributes to the radiative force (see Equations (38)). As a result, the higher

Table 1. Parameters in the simulations. L_γ is the physical luminosity of the fireball (**not the isotropic luminosity**), θ_0 represents the initial size of the fireball, B_0 is the magnetic field at the magnetar surface, n_B represents the radial dependence of the magnetic field (see Equation (39)). The “spectrum” column indicates the initial photon spectrum of the fireball, where “mod BB” is the modified blackbody (Equation (38)), and “BB” is the blackbody (Equation (37)). The “scattering” column shows the adopted scattering process in each model; “magnetic” is the scattering process with the resonant scattering in the magnetic field (see Equations (23)–(26)), and “isotropic” is the case with only the isotropic Thomson scattering. The radius r_{ph} is the analytic photospheric radius normalized with r_0 , and Γ_{ph} is the Lorentz factor at r_{ph} . $L_{X,\text{iso}}$ is the isotropic luminosity of the X-ray, and $L_{\text{kin,iso}}$ is the isotropic kinetic luminosity of the plasma outflow.

| model | L_γ [erg s $^{-1}$] | θ_0 | B_0 [G] | n_B | spectrum | scattering | r_{ph} [r_0] | Γ_{ph} | $L_{X,\text{iso}}$ [erg s $^{-1}$] | $L_{\text{kin,iso}}$ [erg s $^{-1}$] |
|----------|-----------------------------|----------------------|--------------------|-------|----------|------------|---------------------------|----------------------|-------------------------------------|---------------------------------------|
| fiducial | 6.0×10^{39} | 3.1×10^{-2} | 2×10^{14} | -3 | mod BB | magnetic | 1.1 | 1.6 | 3.9×10^{40} | 9.0×10^{32} |
| iso_BB | 6.0×10^{39} | 3.1×10^{-2} | 2×10^{14} | -3 | BB | isotropic | 1.1 | 1.6 | 4.4×10^{40} | 1.2×10^{32} |
| BB | 6.0×10^{39} | 3.1×10^{-2} | 2×10^{14} | -3 | BB | magnetic | 1.1 | 1.6 | 3.6×10^{40} | 7.4×10^{32} |
| B_1e16 | 6.0×10^{39} | 3.1×10^{-2} | 1×10^{16} | -3 | mod BB | magnetic | 1.2 | 1.8 | 3.1×10^{40} | 7.0×10^{32} |
| n_-2 | 6.0×10^{39} | 3.1×10^{-2} | 2×10^{14} | -2 | mod BB | magnetic | 1.1 | 1.6 | 2.8×10^{40} | 2.4×10^{33} |

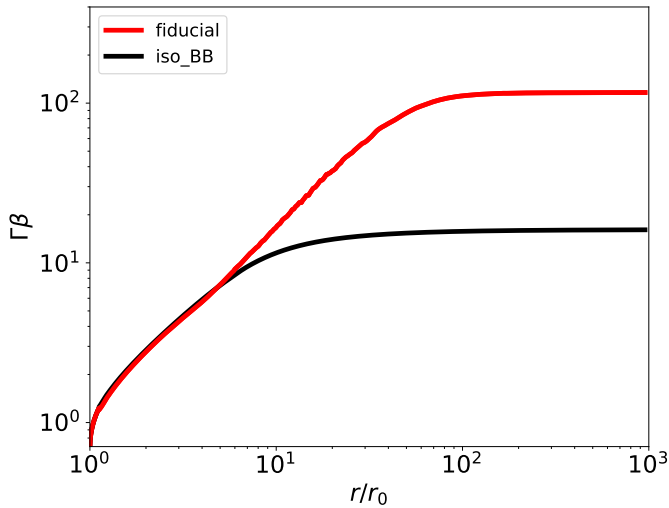


Figure 2. Velocity of the relativistic outflows in the model **fiducial** (red solid line) and the model **iso_BB** (black solid line). The vertical axis is the four-velocity, and the horizontal axis is the radius normalized by the magnetar radius.

terminal velocity is realized in the model **B_1e16**. The stronger the magnetic field, the higher the terminal velocity.

In the model **B_1e16**, the velocity deviates from $\Gamma\beta \propto r$ in $5 \lesssim r/r_0 \lesssim 30$. This is because the scattering cross section of the X-mode photons is suppressed for $\omega \ll \omega_B$ as $\sigma \sim \sigma_T(\omega/\omega_B)^{-2}$ (see Equations (23) and (24)). The condition $\omega \ll \omega_B$ breaks around $r_{\text{res}}/r_0 \sim 34 B_{16}^{1/2} (\hbar\omega)_{0,100\text{keV}}^{-1/2}$ (see Equation (40)), where the ve-

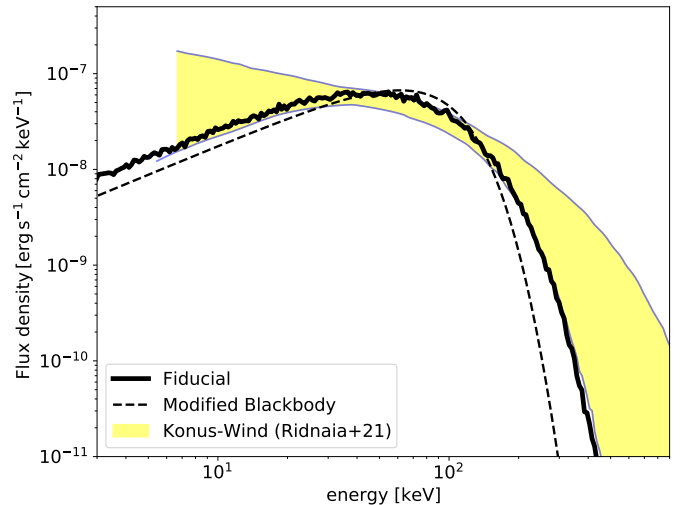


Figure 3. X-ray spectrum in 5–900 keV of the model **fiducial** (thick solid). The vertical axis is the flux density, and the horizontal axis is the photon energy. The black dashed line is the modified blackbody spectrum for reference. The luminosity distance to the magnetar is set to 7 kpc. The yellow-shaded region is the 99.7% error region of the X-ray short burst associated with FRB 20200428A, which is detected from SGR 1935+2154 by the *Konus-Wind* (Ridnaia et al. 2021).

locity again starts to be on the relation $\Gamma\beta \propto r$.² The relation $\Gamma\beta \propto r$ in $r \lesssim 5$ would be sustained by the high photon flux in the inner region. The suppression on the

² If the radiative acceleration is effective, the velocity at a radius, $\Gamma\beta \sim \Gamma_{\text{ph}} r / r_{\text{ph}}$, is completely determined only by the photon field. The photon field at all radii is mainly determined around the photospheric radius. Thus, the radius-velocity relation under the radiative acceleration is also determined around the photospheric radius. Therefore, when the radiative force gets strong again at $r/r_0 \sim 30$, the velocity again returns to the value $\Gamma \sim \Gamma_{\text{ph}}(r/r_{\text{ph}})$ with a more rapid acceleration than $\Gamma \propto r$.

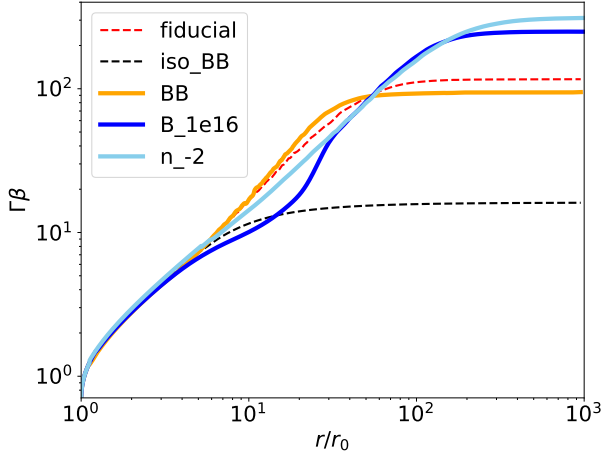


Figure 4. Velocity of the relativistic outflows in all the models. The axes are the same as Figure 2. The dashed red and black lines are the models `fiducial` and `iso_BB`, respectively. The solid orange, blue, and sky blue lines are the models `BB`, `B_1e16`, and `n_-2`.

cross section at $\omega < \omega_B$ alters the acceleration history but does not alter the terminal velocity in this model.

The terminal velocity of the model `n_-2` is higher than that of the model `fiducial` with the same reason in the model `B_1e16`: the magnetic field in the model `n_-2` is stronger than the magnetic field in the model `fiducial` at a given radius. The magnetic field at the surface is the same as that in the model `fiducial`, and the suppression on the cross section shown in the model `B_16` is not significant. Thus, the velocity evolution does not significantly deviate from the relation of $\Gamma\beta \propto r$. The weaker the radial dependence of the magnetic field, the higher the terminal velocity.

Figure 5 shows the parameter dependence of the X-ray spectrum (see Table 1). In the models `BB` and `iso_BB`, as the initial spectrum is the blackbody, the spectrum shapes are significantly different from the other models. Thus, the observed X-ray spectrum in Figure 3 (yellow shaded region) would not be realized with the blackbody spectrum in this scenario. The shape of the X-ray spectrum does not strongly depend on the B_0 and n_B .

3.3. Analytic Estimates

In this subsection, we give analytic estimates to understand the results of the numerical simulations. In Sections 3.3.1 – 3.3.3, we estimate the coasting radius, r_c , where the radiative acceleration ends. We compare the analytic coasting radii and the radius estimated from the simulation results with the condition of $du/d(r/r_0) = 1$. The analytic estimates agree with the numerical results within a factor of two. If we change the definition of the coasting radius as $du/d(r/r_0) = 0.3$, the analytic es-

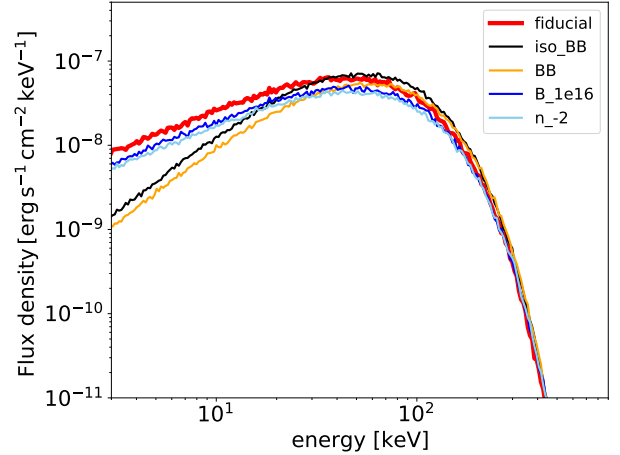


Figure 5. X-ray spectrum in 5–900 keV for all the models. The axes are the same as Figure 3, and the colors are the same as Figure 4.

timates agree with the numerical result within $\sim 15\%$. Since the accelerated plasma follows $\Gamma \sim \Gamma_{\text{ph}} r / r_{\text{ph}}$ in the optically thin regime, the terminal Lorentz factor, Γ_t , is approximately equal to $\Gamma_{\text{ph}} r_c / r_{\text{ph}} \sim 1.5 \times (r_c / r_0)$. In Section 3.3.4, we estimate the optical depth for the resonant scattering.

3.3.1. Thomson Scattering

First, we consider the case of isotropic scattering with the Thomson cross section. The radiative force accelerates the outflow if the work by the radiation during the dynamical time is higher than the rest-mass energy of an electron. The condition for this radiative acceleration is written as

$$\frac{\sigma_{\text{T}} L_{\text{iso}}}{4\pi c \Gamma^2 r^2} \times \frac{r}{\Gamma} > mc^2, \quad (41)$$

where L_{iso} is the isotropic photospheric luminosity. During the radiative acceleration, the Lorentz factor is proportional to the radius (see Figures 2 and 4) (Meszaros et al. 1993; Grimsrud & Wasserman 1998; Li & Sari 2008)

$$\Gamma = \Gamma_{\text{ph}} \frac{r}{r_{\text{ph}}}. \quad (42)$$

Substituting Equation (42) into Equation (41) and setting $\Gamma_{\text{ph}} / r_{\text{ph}} \sim 1$ for simplicity, the coasting radius r_c is estimated as (Nakar et al. 2005)

$$\frac{r_c}{r_0} \simeq \left(\frac{L_{\text{iso}} \sigma_{\text{T}}}{4\pi c^3 m r_0} \right)^{1/4} \sim 12 L_{\text{iso},40}^{1/4} r_{0,6}^{-1/4}. \quad (43)$$

In Figure 4, the black dashed line (the model `iso_BB`) deviate from $\Gamma\beta \propto r$ at $r_c / r_0 \sim 6.7$, which is estimated

with $du/d(r/r_0) = 1$. If we use a “modified” condition $du/d(r/r_0) = 0.3$, $r_c/r_0 \sim 13$ is the coasting radius in the simulation. The terminal velocity of the fluid, which we define as the velocity at $r/r_0 = 10^3$, is $\Gamma\beta \simeq 16$. Equation (43) does not depend on the magnetic field, B_0 and n_B , or the initial temperature of the fireball, T_{ph} . This is because the Thomson cross section is constant.

3.3.2. Resonant Scattering with Blackbody Spectrum

In the case of the blackbody spectrum, the condition for the radiative acceleration with the resonant scattering is written as (Wada & Ioka 2023)

$$\frac{\pi e^2 (L_{\omega, \text{iso}})_{\omega_B}}{2mc^2 r \Gamma^3} > mc^2, \quad (44)$$

where $(L_{\omega, \text{iso}})_{\omega_B} = dL_{\text{iso}}/d\omega|_{\omega=\omega_B}$ is the isotropic specific luminosity of the radiation. Substituting Equations (39) and (42) into Equation (44) and using $T \propto r^{-1}$, where T is the temperature at the comoving frame of the fluid³, we estimate the coasting radius.

For the blackbody spectrum, the isotropic specific luminosity is

$$(L_{\omega, \text{iso}})_{\omega_B} = L_{\text{iso}} \frac{15}{\pi^4} \left(\frac{\hbar\omega_B}{T} \right)^3 \frac{\hbar}{T} \frac{1}{\exp(\hbar\omega_B/T) - 1} \quad (45)$$

Substituting Equations (39), (42), and (45) into Equation (44) and using $T \propto r^{-1}$ and $\exp(z) - 1 \simeq z$ for $z \ll 1$, the coasting radius is (Wada & Ioka 2023)

$$\begin{aligned} \frac{r_c}{r_0} &\simeq \left[\frac{15}{2\pi^3} \frac{\hbar c^2}{m^3 c^6 r_0} L_{\text{ph}} \frac{\bar{B}_0^2}{\bar{T}_{\text{ph}}^3} \left(\frac{r_{\text{ph}}}{r_0 \Gamma_{\text{ph}}} \right)^3 \right]^{\frac{1}{1-2n_B}}, \\ &\sim 45 \times L_{\text{ph},40}^{1/7} B_{0,14.3}^{2/7} \bar{T}_{\text{ph},-1.5}^{-3/7} \quad (\text{for model BB}), \end{aligned} \quad (46)$$

where $\bar{B}_0 = B_0/B_Q$, $\bar{T}_{\text{ph}} = T_{\text{ph}} r_{\text{ph}}/(mc^2 r_0) \sim T_{\text{ph}}/(mc^2)$, $B_Q = m^2 c^3/(\hbar e) = 4.4 \times 10^{13}$ G, and we set $r_{\text{ph}}^{3/7}/(r_0 \Gamma_{\text{ph}})^{3/7} \sim 1$ at the last line for simplicity. In Figure 4, the orange line (the model BB) deviates from $\Gamma\beta \propto r$ at $r_c/r_0 \sim 38$ (52 with the modified condition). The analytic estimate of the coasting radius roughly agrees with the numerical result. The coasting radius strongly depends on the radial dependence of the magnetic field, n_B . The terminal velocity is $\Gamma\beta = 94$. For a larger $|n_B|$, a smaller ω_B makes the specific luminosity at ω_B decrease more rapidly (see Equation (45)),

³ We assume that the shape of the photon spectrum depends only on ω/T and no other parameters appear. In this case, due to the adiabatic cooling of freely streaming photons, the temperature in the expression of the photon spectrum is proportional to r^{-1} (see Li & Sari 2008, for details).

and the radiative force decreases more steeply with radius. This implies that a larger $|n_B|$ leads to a smaller r_c , equivalently a lower terminal Lorentz factor.

3.3.3. Resonant Scattering with Modified Blackbody

The models **fiducial**, **B_1e16**, and **n_-2** adopt the modified blackbody spectrum, for which the isotropic specific luminosity is

$$(L_{\omega, \text{iso}})_{\omega_B} = L_{\text{iso}} \frac{0.073}{T^4} \frac{(\hbar\omega_B)^3}{\exp\left[\frac{(\hbar\omega_B)^2}{T\sqrt{(\hbar\omega_B)^2 + (3\pi^2/5)T^2}}\right] - 1}, \quad (47)$$

where the factor 0.073 is determined by the normalization condition, $\int d\omega L_{\omega, \text{iso}} = L_{\text{iso}}$. Substituting Equations (39), (42), and (47) into Equation (44) and using $T \propto r^{-1}$ and $z \ll 1$, we obtain

$$\begin{aligned} \frac{r_c}{r_0} &= \left[\frac{0.073\sqrt{3}\pi^2}{2\sqrt{5}} \frac{\hbar c^2}{m^3 c^6} \frac{L_0}{r_0} \bar{B}_0 \bar{T}_{\text{ph}}^{-2} \right]^{1/(2-n_B)} \\ &\times \left[\left(\frac{r_0}{r_{\text{ph}}} \right) \left(\frac{r_{\text{ph}}}{r_0 \Gamma_{\text{ph}}} \right)^4 \right]^{1/(2-n_B)} \\ &\sim \begin{cases} 90 \times L_{\text{ph},40}^{1/5} B_{0,14.3}^{1/5} \bar{T}_{\text{ph},-1.5}^{-2/5} & (\text{for model fiducial}) \\ 280 \times L_{\text{ph},40}^{1/4} B_{0,14.3}^{1/4} \bar{T}_{\text{ph},-1.5}^{-1/2} & (\text{for model n_-2}) \end{cases}, \end{aligned} \quad (48)$$

where we set $[r_{\text{ph}}^3/(r_0^3 \Gamma_{\text{ph}}^4)]^{1/(2-n_B)} \sim 1$ at the last line for simplicity. In Figure 4, the red dashed line (the model **fiducial**) deviates from $\Gamma\beta \propto r$ at $r_c/r_0 \sim 53$ (83 with the modified condition) and the sky blue line (the model **n_-2**) deviates from $r_c/r_0 \sim 140$ (260 with the modified condition). The terminal velocity is $\Gamma\beta = 120$ in the model **fiducial** and $\Gamma\beta = 310$ in the model **n_-2**. For the model **B_1e16**, the analytical estimate provides $r_c/r_0 \sim 200$, and the numerical result shows $r/r_0 \sim 120$ (190 with the modified condition). The terminal velocity is $\Gamma\beta = 250$. These analytic estimates roughly agree with the numerical simulations. The soft spectrum in the modified blackbody spectrum leads to a stronger radiative force at a larger radius (see Section 3.2 for details).

3.3.4. Optical Depth for Resonant Scattering

For a photon whose energy is $\hbar\omega$, the resonant scattering is significant in the case that $|1 - \omega_B/\omega| \lesssim \gamma_e$ (see Equations (23)–(26)). This condition gives the radial width Δr_{res} , in which the resonant scattering occurs. Expanding ω_B around ω as $\omega_B \simeq \omega + \Delta r (d\omega_B/dr)|_{\omega_B=\omega}$, and substituting it into $|1 - \omega_B/\omega| \lesssim \gamma_e$, we obtain

$$\Delta r_{\text{res}} \sim \frac{2\alpha}{3|n_B|} \bar{B} r_{\text{res}}, \quad (49)$$

where α is the fine-structure constant, and r_{res} is given by Equation (40). In the radial width of Δr_{res} around $r \sim r_{\text{res}}$, the photons are resonantly scattered with the cross section of $\sim \sigma_T/\gamma_e^2$. During the acceleration, the optical depth for the resonant scattering is

$$\tau_{\text{res}} \sim \frac{\sigma_T}{\gamma_e^2} n_{\pm} \Delta r_{\text{res}} \sim 70 B_{0,14.3}^{-1/2} (\hbar\omega_o)_{100\text{keV}}^{-1/2}, \quad (50)$$

where we use Equations (39), (40), (49), and the conservation of the pair number flux, with $n_B = -3$ and $\Gamma_{\text{ph}} \sim r_{\text{ph}}/r_0 \sim 1$ for simplicity.

4. CONCLUSIONS AND DISCUSSION

In this paper, we numerically study the X-ray radiation, the plasma outflow, and their coupling via the cyclotron resonant scattering in outflowing fireballs responsible for magnetar bursts. For simplicity, we assume a spherically symmetric steady outflow. The plasma is treated as an anisotropic plasma because of the strong synchrotron cooling (Section 2.2). The photon propagation is solved in the magnetized electron-positron pair plasma (Section 2.3). The scattering cross section is suppressed at $\omega < \omega_B$ (except in the case that an O-mode photon is scattered into O-mode), and photons of both the two modes satisfying $\omega \sim \omega_B$ are resonantly scattered. We solve the plasma outflow and the radiation iteratively and find the steady solution of the plasma and radiation.

We apply our model to the X-ray short burst from a magnetar associated with the Galactic FRB, FRB 20200428A (Section 3.1). The X-ray spectrum observed by the *Konus-Wind* is reproduced by the Compton up-scattering in the relativistic outflow and the superposition of the radiation components with different beaming factors with the suitable parameters (Figure 3). The plasma outflow is accelerated by the radiative force, and the four-velocity is ~ 100 (Figure 2). This velocity is two orders of magnitude higher than the outflow without the radiative acceleration in the optically thin region and is one order of magnitude higher than the outflow without the cyclotron resonant scattering.

We also comprehensively study the radiative acceleration via the resonant scattering numerically and analytically (Section 3.2 and 3.3). We showed that the strong magnetic field enhances the terminal velocity of the outflow, and the initial spectrum does not strongly change the terminal velocity in the models of our simulation (Figure 4). These numerical results are roughly consistent with our analytic estimate (Section 3.3).

Our numerical simulations show that a relativistic outflow with $\Gamma \sim 100$ is always created in the outflowing fireball near the magnetic pole. Such a relativistic outflow can be the source for Galactic FRB 20200428A associated with the magnetar short burst (Wada & Ioka 2023). In our simulation, we consider pure electron-positron pair fireballs, and the resultant kinetic energy of the outflow is much lower than the energy of FRBs. Even in fireballs with baryons, a relativistic outflow with $\Gamma \sim 100$ is analytically predicted in Wada & Ioka (2023). The kinetic luminosity of the relativistic outflow can be $1\text{--}10^3$ times higher than the observed FRB luminosities (Figure 6 of Wada & Ioka 2023). Baryons in fireballs can also change the polarization of X-ray bursts because the normal modes and the cross sections in the pair plasma and in the baryonic plasma are different. The circular polarization of the X-ray bursts can provide clues to the amount of baryons, and possibly to the trigger mechanism of the bursts (Wada & Shimoda 2024). Motivated by the above discussion, the baryon-loaded fireball will be investigated in our next paper.

In our simulations, the curvature effect of the magnetic field lines is not taken into account. The outflow near the outer edge of the fireball can be decelerated by the radiation (Beloborodov 2013). In such a case, the X-ray spectrum may be harder than our results (Lundman et al. 2013; Ito et al. 2013) due to scatterings in a shear flow. We need 2D simulations to include this curvature effect. This subject is also left as our future studies.

ACKNOWLEDGEMENTS

We thank K. Ioka, K. Kashiyama, K. Murase, W. Ishizaki, K. Kawaguchi, T. Kawashima, H. Ito, and A. Suzuki for fruitful discussions and comments. We also thank R. Goto, Y. Ichinose, T. Kinugawa, Y. Kusafuka, K. Nishiwaki, J. Shimoda for daily discussions. This work is supported by Grants-in-Aid for Scientific Research, No. 22K20366 (TW), Nos. 22K03684, and 23H04899 (KA), from the Ministry of Education, Culture, Sports, Science and Technology (MEXT) of Japan. Our study is also supported by the joint research program of the Institute for Cosmic Ray Research (ICRR), the University of Tokyo. Numerical computation in this work was carried out at the Yukawa Institute Computer Facility.

REFERENCES

- Abramowicz, M. A., Novikov, I. D., & Paczynski, B. 1991, *ApJ*, 369, 175, doi: [10.1086/169748](https://doi.org/10.1086/169748)
- Asano, K., & Takahara, F. 2007, *ApJ*, 655, 762, doi: [10.1086/509756](https://doi.org/10.1086/509756)

- . 2009, *ApJL*, 690, L81, doi: [10.1088/0004-637X/690/1/L81](https://doi.org/10.1088/0004-637X/690/1/L81)
- Beloborodov, A. M. 2011, *ApJ*, 737, 68, doi: [10.1088/0004-637X/737/2/68](https://doi.org/10.1088/0004-637X/737/2/68)
- . 2013, *ApJ*, 762, 13, doi: [10.1088/0004-637X/762/1/13](https://doi.org/10.1088/0004-637X/762/1/13)
- Bochenek, C. D., Ravi, V., Belov, K. V., et al. 2020, *Nature*, 587, 59, doi: [10.1038/s41586-020-2872-x](https://doi.org/10.1038/s41586-020-2872-x)
- Boggs, S. E., Zoglauer, A., Bellm, E., et al. 2007, *ApJ*, 661, 458, doi: [10.1086/516732](https://doi.org/10.1086/516732)
- Canfield, E., Howard, W. M., & Liang, E. P. 1987, *ApJ*, 323, 565, doi: [10.1086/165853](https://doi.org/10.1086/165853)
- Canuto, V., Lodenquai, J., & Ruderman, M. 1971, *PhRvD*, 3, 2303, doi: [10.1103/PhysRevD.3.2303](https://doi.org/10.1103/PhysRevD.3.2303)
- Chandrasekhar, S. 1960, Radiative transfer
- Chew, G. F., Goldberger, M. L., & Low, F. E. 1956, *Proceedings of the Royal Society of London Series A*, 236, 112, doi: [10.1098/rspa.1956.0116](https://doi.org/10.1098/rspa.1956.0116)
- Chhotray, A., & Lazzati, D. 2018, *MNRAS*, 476, 2352, doi: [10.1093/mnras/sty286](https://doi.org/10.1093/mnras/sty286)
- CHIME/FRB Collaboration, Andersen, B. C., Bandura, K. M., et al. 2020, *Nature*, 587, 54, doi: [10.1038/s41586-020-2863-y](https://doi.org/10.1038/s41586-020-2863-y)
- Cordes, J. M., & Chatterjee, S. 2019, *ARA&A*, 57, 417, doi: [10.1146/annurev-astro-091918-104501](https://doi.org/10.1146/annurev-astro-091918-104501)
- Demidov, I., & Lyubarsky, Y. 2023, *MNRAS*, 518, 810, doi: [10.1093/mnras/stac3120](https://doi.org/10.1093/mnras/stac3120)
- Dolence, J. C., Gammie, C. F., Mościbrodzka, M., & Leung, P. K. 2009, *ApJS*, 184, 387, doi: [10.1088/0067-0049/184/2/387](https://doi.org/10.1088/0067-0049/184/2/387)
- Duncan, R. C., & Thompson, C. 1992, *ApJL*, 392, L9, doi: [10.1086/186413](https://doi.org/10.1086/186413)
- Einfeldt, B. 1988, *SIAM Journal on Numerical Analysis*, 25, 294, doi: [10.1137/0725021](https://doi.org/10.1137/0725021)
- Enoto, T., Kisaka, S., & Shibata, S. 2019, *Reports on Progress in Physics*, 82, 106901, doi: [10.1088/1361-6633/ab3def](https://doi.org/10.1088/1361-6633/ab3def)
- Gedalin, M. 1991, *Physics of Fluids B*, 3, 1871, doi: [10.1063/1.859656](https://doi.org/10.1063/1.859656)
- Gedalin, M., & Oiberman, I. 1995, *PhRvE*, 51, 4901, doi: [10.1103/PhysRevE.51.4901](https://doi.org/10.1103/PhysRevE.51.4901)
- Goodman, J. 1986, *ApJL*, 308, L47, doi: [10.1086/184741](https://doi.org/10.1086/184741)
- Grimsrud, O. M., & Wasserman, I. 1998, *MNRAS*, 300, 1158, doi: [10.1046/j.1365-8711.1998.02004.x](https://doi.org/10.1046/j.1365-8711.1998.02004.x)
- Harding, A. K., & Lai, D. 2006, *Reports on Progress in Physics*, 69, 2631, doi: [10.1088/0034-4885/69/9/R03](https://doi.org/10.1088/0034-4885/69/9/R03)
- Herold, H. 1979, *PhRvD*, 19, 2868, doi: [10.1103/PhysRevD.19.2868](https://doi.org/10.1103/PhysRevD.19.2868)
- Hurley, K., Cline, T., Mazets, E., et al. 1999, *Nature*, 397, 41, doi: [10.1038/16199](https://doi.org/10.1038/16199)
- Hurley, K., Boggs, S. E., Smith, D. M., et al. 2005, *Nature*, 434, 1098, doi: [10.1038/nature03519](https://doi.org/10.1038/nature03519)
- Ioka, K. 2020, *ApJL*, 904, L15, doi: [10.3847/2041-8213/abc6a3](https://doi.org/10.3847/2041-8213/abc6a3)
- Ito, H., Nagataki, S., Ono, M., et al. 2013, *ApJ*, 777, 62, doi: [10.1088/0004-637X/777/1/62](https://doi.org/10.1088/0004-637X/777/1/62)
- Iwamoto, S., & Takahara, F. 2004, *ApJ*, 601, 78, doi: [10.1086/380300](https://doi.org/10.1086/380300)
- Kaspi, V. M., & Beloborodov, A. M. 2017, *ARA&A*, 55, 261, doi: [10.1146/annurev-astro-081915-023329](https://doi.org/10.1146/annurev-astro-081915-023329)
- Katz, J. I. 2018, *Progress in Particle and Nuclear Physics*, 103, 1, doi: [10.1016/j.pnpnp.2018.07.001](https://doi.org/10.1016/j.pnpnp.2018.07.001)
- . 2020, *MNRAS*, 499, 2319, doi: [10.1093/mnras/staa3042](https://doi.org/10.1093/mnras/staa3042)
- Kawaguchi, K., Fujibayashi, S., & Shibata, M. 2023, *PhRvD*, 107, 023026, doi: [10.1103/PhysRevD.107.023026](https://doi.org/10.1103/PhysRevD.107.023026)
- Lazzati, D. 2016, *ApJ*, 829, 76, doi: [10.3847/0004-637X/829/2/76](https://doi.org/10.3847/0004-637X/829/2/76)
- Li, C., & Sari, R. 2008, *ApJ*, 677, 425, doi: [10.1086/527551](https://doi.org/10.1086/527551)
- Li, C. K., Lin, L., Xiong, S. L., et al. 2021, *Nature Astronomy*, doi: [10.1038/s41550-021-01302-6](https://doi.org/10.1038/s41550-021-01302-6)
- Li, X., Ge, M., Lin, L., et al. 2022, *ApJ*, 931, 56, doi: [10.3847/1538-4357/ac6587](https://doi.org/10.3847/1538-4357/ac6587)
- Lifshitz, E. M., & Pitaevskii, L. P. 1981, *Physical kinetics*
- Lindquist, R. W. 1966, *Annals of Physics*, 37, 487, doi: [10.1016/0003-4916\(66\)90207-7](https://doi.org/10.1016/0003-4916(66)90207-7)
- Lorimer, D. R., Bailes, M., McLaughlin, M. A., Narkevic, D. J., & Crawford, F. 2007, *Science*, 318, 777, doi: [10.1126/science.1147532](https://doi.org/10.1126/science.1147532)
- Lu, W., Kumar, P., & Zhang, B. 2020, *MNRAS*, 498, 1397, doi: [10.1093/mnras/staa2450](https://doi.org/10.1093/mnras/staa2450)
- Lundman, C., Pe'er, A., & Ryde, F. 2013, *MNRAS*, 428, 2430, doi: [10.1093/mnras/sts219](https://doi.org/10.1093/mnras/sts219)
- Lyubarskii, Y. É. 1986, *Astrophysics*, 25, 577, doi: [10.1007/BF01006289](https://doi.org/10.1007/BF01006289)
- Lyubarsky, Y. E. 2002, *MNRAS*, 332, 199, doi: [10.1046/j.1365-8711.2002.05290.x](https://doi.org/10.1046/j.1365-8711.2002.05290.x)
- Lyutikov, M. 2021, *arXiv e-prints*, arXiv:2110.08435, <https://arxiv.org/abs/2110.08435>
- Martí, J. M., & Müller, E. 2003, *Living Reviews in Relativity*, 6, 7, doi: [10.12942/lrr-2003-7](https://doi.org/10.12942/lrr-2003-7)
- Mereghetti, S., Savchenko, V., Ferrigno, C., et al. 2020, *ApJL*, 898, L29, doi: [10.3847/2041-8213/aba2cf](https://doi.org/10.3847/2041-8213/aba2cf)
- Meszaros, P. 1992, *High-energy radiation from magnetized neutron stars* (University of Chicago press)
- Meszaros, P., Laguna, P., & Rees, M. J. 1993, *ApJ*, 415, 181, doi: [10.1086/173154](https://doi.org/10.1086/173154)
- Mihalas, D., & Mihalas, B. W. 1984, *Foundations of radiation hydrodynamics*
- Nagel, W. 1981, *ApJ*, 251, 288, doi: [10.1086/159464](https://doi.org/10.1086/159464)

- Nakar, E., Piran, T., & Sari, R. 2005, *ApJ*, 635, 516, doi: [10.1086/497296](https://doi.org/10.1086/497296)
- Paczynski, B. 1986, *ApJL*, 308, L43, doi: [10.1086/184740](https://doi.org/10.1086/184740)
- Petroff, E., Hessels, J. W. T., & Lorimer, D. R. 2019, *A&A Rv*, 27, 4, doi: [10.1007/s00159-019-0116-6](https://doi.org/10.1007/s00159-019-0116-6)
- . 2021, arXiv e-prints, arXiv:2107.10113. <https://arxiv.org/abs/2107.10113>
- Piran, T. 1999, *PhR*, 314, 575, doi: [10.1016/S0370-1573\(98\)00127-6](https://doi.org/10.1016/S0370-1573(98)00127-6)
- Platts, E., Weltman, A., Walters, A., et al. 2019, *PhR*, 821, 1, doi: [10.1016/j.physrep.2019.06.003](https://doi.org/10.1016/j.physrep.2019.06.003)
- Platts, E., Caleb, M., Stappers, B. W., et al. 2021, *MNRAS*, 505, 3041, doi: [10.1093/mnras/stab1544](https://doi.org/10.1093/mnras/stab1544)
- Pozdnyakov, L. A., Sobol, I. M., & Syunyaev, R. A. 1983, *Astrophys. Space Phys. Res.*, 2, 189
- Ridnaia, A., Svinkin, D., Frederiks, D., et al. 2021, *Nature Astronomy*, 5, 372, doi: [10.1038/s41550-020-01265-0](https://doi.org/10.1038/s41550-020-01265-0)
- Roe, P. L. 1986, *Annual Review of Fluid Mechanics*, 18, 337, doi: [10.1146/annurev.fl.18.010186.002005](https://doi.org/10.1146/annurev.fl.18.010186.002005)
- Ryan, B. R., Dolence, J. C., & Gammie, C. F. 2015, *ApJ*, 807, 31, doi: [10.1088/0004-637X/807/1/31](https://doi.org/10.1088/0004-637X/807/1/31)
- Ryde, F., Lundman, C., & Acuner, Z. 2017, *MNRAS*, 472, 1897, doi: [10.1093/mnras/stx2019](https://doi.org/10.1093/mnras/stx2019)
- Sasaki, S. 1958, *Tohoku Mathematical Journal, Second Series*, 10, 338
- . 1962, *Tohoku Mathematical Journal, Second Series*, 14, 146
- Schneider, V., Katscher, U., Rischke, D. H., et al. 1993, *Journal of Computational Physics*, 105, 92, doi: [10.1006/jcph.1993.1056](https://doi.org/10.1006/jcph.1993.1056)
- Shemi, A., & Piran, T. 1990, *ApJL*, 365, L55, doi: [10.1086/185887](https://doi.org/10.1086/185887)
- Tavani, M., Casentini, C., Ursi, A., et al. 2021, *Nature Astronomy*, 5, 401, doi: [10.1038/s41550-020-01276-x](https://doi.org/10.1038/s41550-020-01276-x)
- Thompson, C., & Duncan, R. C. 1995, *MNRAS*, 275, 255, doi: [10.1093/mnras/275.2.255](https://doi.org/10.1093/mnras/275.2.255)
- . 1996, *ApJ*, 473, 322, doi: [10.1086/178147](https://doi.org/10.1086/178147)
- . 2001, *ApJ*, 561, 980, doi: [10.1086/323256](https://doi.org/10.1086/323256)
- Thornton, D., Stappers, B., Bailes, M., et al. 2013, *Science*, 341, 53, doi: [10.1126/science.1236789](https://doi.org/10.1126/science.1236789)
- van Leer, B. 1979, *Journal of Computational Physics*, 32, 101, doi: [10.1016/0021-9991\(79\)90145-1](https://doi.org/10.1016/0021-9991(79)90145-1)
- van Putten, T., Watts, A. L., Baring, M. G., & Wijers, R. A. M. J. 2016, *MNRAS*, 461, 877, doi: [10.1093/mnras/stw1279](https://doi.org/10.1093/mnras/stw1279)
- Ventura, J. 1979, *PhRvD*, 19, 1684, doi: [10.1103/PhysRevD.19.1684](https://doi.org/10.1103/PhysRevD.19.1684)
- Wada, T., & Ioka, K. 2023, *MNRAS*, 519, 4094, doi: [10.1093/mnras/stac3681](https://doi.org/10.1093/mnras/stac3681)
- Wada, T., & Shimoda, J. 2024, arXiv e-prints, arXiv:2401.16783, doi: [10.48550/arXiv.2401.16783](https://doi.org/10.48550/arXiv.2401.16783)
- Yamasaki, S., Kashiyama, K., & Murase, K. 2022, *MNRAS*, 511, 3138, doi: [10.1093/mnras/stac234](https://doi.org/10.1093/mnras/stac234)
- Yamasaki, S., Lyubarsky, Y., Granot, J., & Göğüş, E. 2020, *MNRAS*, 498, 484, doi: [10.1093/mnras/staa2223](https://doi.org/10.1093/mnras/staa2223)
- Yang, Y.-P., & Zhang, B. 2015, *ApJ*, 815, 45, doi: [10.1088/0004-637X/815/1/45](https://doi.org/10.1088/0004-637X/815/1/45)
- . 2021, *ApJ*, 919, 89, doi: [10.3847/1538-4357/ac14b5](https://doi.org/10.3847/1538-4357/ac14b5)
- Zhang, B. 2018, *The Physics of Gamma-Ray Bursts* (Cambridge University Press), doi: [10.1017/9781139226530](https://doi.org/10.1017/9781139226530)
- . 2020a, *Nature*, 582, 344, doi: [10.1038/d41586-020-01713-x](https://doi.org/10.1038/d41586-020-01713-x)
- . 2020b, *Nature*, 587, 45, doi: [10.1038/s41586-020-2828-1](https://doi.org/10.1038/s41586-020-2828-1)

APPENDIX

A. DERIVATION OF RADIATIVE FORCE

Here, we derive the radiative force in Equation (29). We assume that electrons are cold, no absorption nor emission occurs, the cross section is given by Equations (23)–(26), and the spacetime is flat. In this part, the photon distribution function $F_\gamma(x^\mu, \vec{p})$ is denoted as $F(x, p)$ for notation simplicity.

The radiative force is written as (Lindquist 1966)

$$G^\nu = \int d\Pi p^\nu \left(\frac{dF}{d\lambda} \right)_{\text{coll}}. \quad (\text{A1})$$

Using Equation (20), this is rewritten as

$$G^\nu = \frac{\rho(x)}{m} \int d\Pi p^\nu \left[\int d\Pi' \kappa(x, p') \zeta(x; p' \rightarrow p) F(x, p') - \kappa(x, p) F(x, p) \right]. \quad (\text{A2})$$

This expression is valid in any coordinate system. For elastic scatterings, the invariant phase function in the fluid rest frame is (Lindquist 1966)

$$\zeta(x; p' \rightarrow p) = \frac{P_{\text{ang}}(\cos \theta, \cos \theta')}{4\pi} \frac{\delta(p'^{(t)} - p^{(t)})}{p^{(t)}}, \quad (\text{A3})$$

where θ is the angle between the magnetic field and the wavevector of the scattered photon in the electron rest frame, θ' is that of the incident photon, and $P_{\text{ang}}(\cos \theta, \cos \theta')$ is the angular dependence of the scattering angle, which satisfies $\int d\Omega P_{\text{ang}}(\cos \theta, \cos \theta')/(4\pi) = 1$. The superscript (t) represents the 0th component of the four-momentum in the fluid comoving frame. Substituting Equation (A3) into Equation (A2), the first term in Equation (A2) is

$$\begin{aligned} \int d\Pi p^\nu \int d\Pi' \kappa(x, p') \zeta(x; p' \rightarrow p) F(x, p') &= \int d\Pi p^\nu \int d\Pi' \kappa(x, p') F(x, p') \frac{P_{\text{ang}}(\cos \theta, \cos \theta')}{4\pi} \frac{\delta(p'^{(t)} - p^{(t)})}{p^{(t)}} \\ &= \int p^{(t)} dp^{(t)} d\Omega d\Omega' \kappa(x, p') F(x, p') p^\nu \frac{P_{\text{ang}}(\cos \theta, \cos \theta')}{4\pi}. \end{aligned} \quad (\text{A4})$$

In the comoving frame of the fluid, we can set $p^{(\nu)} = p^{(t)}(1, \sin \theta \cos \phi, \sin \theta \sin \phi, \cos \theta)$ without losing generality because $p^{(t)}$, θ , and ϕ are the integral variables. If $P_{\text{ang}}(\cos \theta, \cos \theta')$ is even function of $\cos \theta$ as Equations (23)–(26),

$$\int d\Omega p^{(t)} \frac{P_{\text{ang}}(\cos \theta, \cos \theta')}{4\pi} = p^{(t)} = -(p^\mu u_\mu), \quad (\text{A5})$$

$$\int d\Omega p^{(i)} \frac{P_{\text{ang}}(\cos \theta, \cos \theta')}{4\pi} = 0 \quad (i = 1, 2, 3), \quad (\text{A6})$$

where we have used the normalization condition on $P_{\text{ang}}(\cos \theta, \cos \theta')$. The Equation (A4) in the comoving frame is rewritten as

$$\begin{aligned} \int d\Pi p^{(\nu)} \int d\Pi' \kappa(x, p') \zeta(x; p' \rightarrow p) F(x, p') &= \int p^{(t)} dp^{(t)} d\Omega' \kappa(x, p') F(x, p') (-p^\mu u_\mu) \delta_{(t)}^{(\nu)}, \\ &= \int d\Pi \kappa(x, p) F(x, p) (-p^\mu u_\mu) u^{(\nu)}, \end{aligned} \quad (\text{A7})$$

where we have rewritten the integral variables for angles to be unprimed. Using Equations (A2) and (A7), the radiative force in the comoving frame is

$$G^{(\nu)} = \frac{\rho(x)}{m} \int d\Pi \kappa(x, p) F(x, p) \left[-p^{(\nu)} - (p^\mu u_\mu) u^{(\nu)} \right], \quad (\text{A8})$$

and in any frame, the radiative force is written as

$$\begin{aligned}
 G^\nu &= \frac{\rho(x)}{m} \int d\Pi \kappa(x, p) F(x, p) [-p^\nu - (p^\mu u_\mu) u^\nu] \\
 &= -\frac{\rho(x)}{m} h_\mu^\nu \int d\Pi p^\mu \kappa(x, p) F(x, p).
 \end{aligned}
 \tag{A9}$$